AGU PUBLICATIONS

JGR

Journal of Geophysical Research: Oceans

RESEARCH ARTICLE

10.1002/2014JC010146

Vertical structure of eddies and Rossby waves, and their effect on the Atlantic meridional overturning circulation at 26.5°N

L. Clément[1], E. Frajka-Williams[1], Z. B. Szuts[2], and S. A. Cunningham[3]

[1]National Oceanography Centre, University of Southampton, Waterfront Campus, Southampton, UK, [2]Applied Physics Laboratory, University of Washington, Seattle, Washington, USA, [3]Scottish Association of Marine Science, Argyll, Scotland

Key Points:
- Eddies/Rossby waves explain 42% of the upper mid-ocean transport variance
- Eddies/Rossby waves exhibit first baroclinic mode structure at 80–250 day periods
- At the boundary, higher baroclinic modes also contain substantial energy

Correspondence to:
L. Clément,
clement.louis@gmail.com

Citation:
Clément, L., E. Frajka-Williams, Z. B. Szuts, and S. A. Cunningham (2014), Vertical structure of eddies and Rossby waves, and their effect on the Atlantic meridional overturning circulation at 26.5°N, *J. Geophys. Res. Oceans*, *119*, 6479–6498, doi:10.1002/2014JC010146.

Received 21 MAY 2014
Accepted 29 AUG 2014
Accepted article online 3 SEP 2014
Published online 24 SEP 2014

Abstract The meridional overturning circulation (MOC) at 26.5°N in the Atlantic has a standard deviation of 4.9 Sv and contains large fluctuations at subannual periods. The geostrophic component of the MOC is believed to be influenced on subannual time scales by eddies and Rossby waves. To quantify this effect, the vertical structure and surface characteristics of westward propagating signals are studied using altimetric data and full-depth mooring measurements from the RAPID array at 26.5°N. Westward propagating features are observed in the western North Atlantic in both data sets and have periods of 80–250 days in the first baroclinic mode. These features are still observed by the RAPID moorings 20 km offshore of the western boundary. The western boundary also exhibits deep variability characterized by enhanced energy in higher baroclinic modes. The effect of eddies and Rossby waves on the geostrophic transport is quantified by representing their vertical structure with the first baroclinic mode. In total, 42% of the variance of the transbasin thermocline transport inferred from geostrophic calculations at 26.5°N can be attributed to first mode variability, which is associated with eddies and Rossby waves at periods of 80–250 days. The standard deviation of the transbasin thermocline transport due to eddies and Rossby waves is estimated to be 2.6 Sv.

1. Introduction

The Atlantic meridional overturning circulation (MOC) plays a significant role in redistributing heat from the equator to higher latitudes [*Hall and Bryden*, 1982]. An understanding of the MOC variability is essential to comprehend the fluctuations of the mild European climate [*Pohlmann et al*., 2006], to assess its link with the abrupt climate change of glacial cycles [*Broecker*, 2003], and to evaluate the effect of increased greenhouse gases [*Gregory et al*., 2005]. Despite earlier expectations of a slowly varying MOC, continuous measurements since 2004 have found significant short-term variability [*Cunningham et al*., 2007] that needs to be better understood to accurately interpret potential long-term changes.

For instance, prior to continuous measurements, transbasin hydrographic surveys occupied every 5–10 years were used to investigate large-scale and low-frequency circulation. Using five transatlantic sections at 24°N in the Atlantic, *Bryden et al*. [2005b] found a 30% decrease in the MOC from 1957 to 2004. This reduction was associated with an increased southward upper mid-ocean transport and a decreased southward lower North Atlantic deep water. The amplitude of the reduction was close to the eddy uncertainty of ±6 Sv estimated using inverse calculations from similar hydrographic sections [*Ganachaud*, 2003]. However, a thermocline temperature anomaly extending several hundred kilometers off the western boundary and an unequal transport anomaly in the upper and lower North Atlantic deep waters led *Bryden et al*. [2005b] to discard an eddy-induced explanation. In addition, the continuous measurement of the MOC provided by the RAPID program [*Cunningham et al*., 2007] raised the question of what processes contribute to the subannual MOC variability, which is estimated to be 4.9 Sv around a mean of 18.7 Sv ($1\text{Sv}=10^6\text{m}^3\text{s}^{-1}$) for the period 2004–2011. *Kanzow et al*. [2010] attributed most of the decline observed in *Bryden et al*. [2005b] to the seasonality of the MOC. This seasonality with an amplitude of 5.9 Sv is visible in the upper mid-ocean and mostly originates from density changes at the eastern boundary following wind-stress curl anomalies [*Chidichimo et al*., 2010]. While the transport anomaly observed by *Bryden et al*. [2005b] in 2004 is less anomalous when adjusting for the seasonality of the upper mid-ocean transport found by *Kanzow et al*. [2010], the remaining anomalous transport was localized at the western boundary which is a region of more significant eddy activity than the eastern boundary. Despite the contribution of the MOC seasonality to the MOC subannual variability, the quantification of the eddy effect on the geostrophic transport still needs to be determined.

Following the observation of the subannual MOC variability in *Cunningham et al*. [2007], several studies investigated the effect of Rossby waves on the meridional circulation. Using an eddy-permitting model, *Hirschi et al*. [2007] attributed 3–4 Sv of variability to Rossby waves through the thermal wind relation. In contrast, *Kanzow et al*. [2009] analyzed the RAPID measurements and suggested that the MOC variability is not strongly affected by these features because their energy decreases with proximity to the boundary. In particular for interannual to decadal timescales, *Kanzow et al*. [2009] determined that eddies do not dominate the MOC variability. Their main argument, reinforced by *Bryden et al*. [2009], comes from the observation of a threefold decrease of rms sea surface height anomaly (SSHA) and dynamic height anomaly (DHA) from 100 to 20 km offshore of the western boundary. The reduced variability was explained by an export of the eddy transport variability through boundary-trapped waves. *Kanzow et al*. [2009] calculated the upper bound of the transport variability attributed to eddies to be 4.2 Sv using SSHA from 1992 to 2008 to characterize the decrease of eddy variability at the boundary. This is in contrast to *Wunsch* [2008] who found 16 Sv without taking into account the observed SSHA rms decrease at the western boundary. A characterization of the vertical structure of propagating signals would help to refine the amplitude of their influence on the MOC.

The vertical structure of eddies has been investigated in the North Atlantic over the past few decades. *Parker* [1971] described Gulf Stream rings which were coherent over the full water column in the Sargasso Sea. Extensive research was conducted in the 1970s to understand the dynamics of eddies, and their vertical structure was characterized by a first baroclinic mode over flat topography as part of the POLYGONE, MODE, and POLYMODE projects [*Richman et al*., 1977; *MODE Group*, 1978]. The development of altimetry through the past decades considerably extended the global observations and understanding of eddy dynamics. Meanwhile, Rossby waves were first observed at the ocean surface [*Chelton and Schlax*, 1996] once it was possible to reduce tidal effects from altimetric data. Though eddies and Rossby waves are two distinct processes, their common properties of westward phase speeds, surface and subsurface signatures render their observational distinction more challenging [*Chelton et al*., 2007]. Altimetry confirmed the picture of a highly turbulent ocean with westward propagating anomalies able to transfer energy across the ocean. Since the development of altimeters, it became essential to establish the link between SSHA and subsurface variability to understand the dynamics of westward propagating signals and their effect on large scale circulation. Using a modal decomposition, *Stammer* [1997] and *Wunsch* [1997] found that the first baroclinic mode, intensified in the thermocline, was the most representative mode of enhanced surface kinetic energy. The RAPID mooring array provides a new data set with which to investigate eddy and Rossby wave variability in three dimensions: zonal, vertical, and temporal. *Szuts et al*. [2012] studied the vertical structure of fluctuations in the full-height RAPID mooring data and their correlation with SSHA. They observed a strong link between the first baroclinic mode and SSHA variability in the ocean interior; a link which weakened toward the boundary. It is still necessary to investigate zonal propagation to connect mooring observations with the altimetric signature of propagating signals.

The aim of the present study is to characterize westward propagating signals (including eddies and Rossby waves) at 26.5°N and to evaluate their effect on the variability of the MOC. A clear identification of processes involved in the short-term variability of the MOC will help to better detect its long-term climatic trend. For estimating North Atlantic transport, the RAPID array provides a 7 year-long continuous record from 2004 to 2011 with twice daily measurements. First, westward propagating SSHA signals at 26.5°N are studied (section 3.1). Their surface characteristics are then related to subsurface variability (section 3.2), and a normal mode decomposition is applied to establish their vertical structure at the western boundary of the mooring array (section 3.3). Once density anomalies are attributed to eddies or Rossby waves, the final step is to quantify their influence on the geostrophic meridional transport (section 4). This analysis also sheds light on the vertical structure of westward propagating signals as they approach the boundary.

2. Data and Methods

2.1. Mooring Observations

The array of full-depth moorings at the western boundary includes four moorings Wb2, Wb3, Wb4, and Wb5 located at 20, 49, 108, and 500 km offshore and in water depths of 3900, 4840, 4700, and 5300 m, respectively (Figure 1). Each mooring is equipped with a set of SBE37 MicroCAT instruments (Sea-Bird

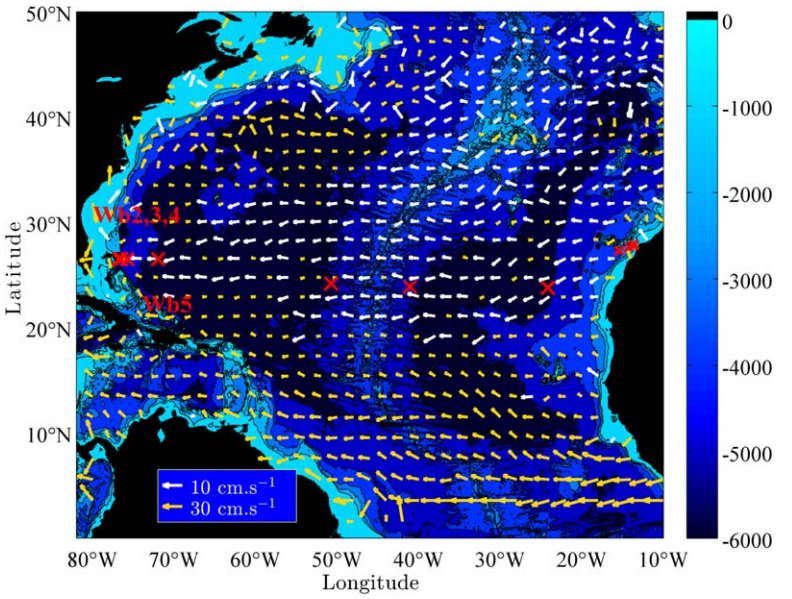

Figure 1. Speed and direction (arrows) of surface propagations in the North Atlantic inferred from time space maximum lagged correlation of sea surface height anomaly between March 2004 to January 2011 over bathymetry (colorscale). The RAPID array mooring positions are indicated in red crosses with the western boundary moorings Wb2, Wb3, Wb4, and Wb5. The bathymetry comes from the ETOPO1 data set provided by the National Oceanic and Atmospheric Administration (NOAA).

Electronics, Bellevue, WA, USA) which measure temperature, conductivity, and pressure profiles from April 2004 to January 2011. The short duration record available at Wb4, which only starts in 2008, limits the utility of Wb4 in most of our analyses. The vertical spacing between instruments is approximately 100 m in the shallowest 500 m, then 200 m from 500 to 1000 m, and 500 m below 1000 m, giving a total of about 15 instruments [*Rayner et al*., 2011]. MicroCAT CTDs are calibrated before and after each deployment against a lowered CTD package to improve their accuracy to 0.001°C for temperature, 0.002 psu for salinity, and 5–10 dbar for pressure. Data are sampled by CTDs every 30 mins. They are 2 day low-pass filtered using a sixth-order Butterworth filter to remove high-frequency variability (e.g., tides or inertial oscillations). They are then subsampled every 12 h. Hydrographic data are interpolated every 20 dbar using climatologies of vertical temperature and salinity gradients as a function of temperature, following the method described in *Johns et al*. [2005].

Using neutral densities (γ^n), isopycnal displacements $\zeta(z,t)$ are calculated following *Desaubies and Gregg* [1981] as the vertical displacement of isopycnals from their time-mean depth $\bar{z}(\gamma^n)$,

$$\zeta(\bar{z}(\gamma^n),t)=z(\gamma^n,t)-\bar{z}(\gamma^n). \quad (1)$$

The conversion from $\zeta(\bar{z}(\gamma^n),t)$ to $\zeta(z,t)$ requires a monotonic density profile at each mooring obtained with the use of neutral densities instead of potential densities, which are nonmonotonic in the western North Atlantic [*Lynn and Reid*, 1968]. Dynamic height anomalies (DHA) are calculated by integrating specific volume from the bottom to 140 m. Omitting the top 140 m [*Szuts et al*., 2012] reduces the impact of uneven sampling of the surface layer from deployment to deployment and minimizes the effect of seasonal heat fluxes on our analysis [*Gill and Niiler*, 1973].

To localize each mooring relative to the mean currents and topography, data from western boundary current meter arrays [*Bryden et al*., 2005a] prior to the RAPID program (1986–1997) were used to create a mean velocity section east of the Bahamas (Figure 2). Unlike the RAPID array, which only uses current meters at and west of Wb4, these arrays extended 500 km offshore. As described in *Bryden et al*. [2005a] and *Johns et al*. [2008], the strong southward flowing Deep Western Boundary Current (DWBC) is observed from 1000 to 4800 dbar with a maximum of 15 cm s^{-1} at 2000 m located 55 km offshore and a secondary maximum at 1200 m situated 20 km offshore. Two escarpments, extending from the continental shelf at 26.6 and 26.7°N, shelter Wb2 from the deep velocity maximum of the DWBC below 1600 m [*Johns et al*., 2008]. The deep northward recirculation, from 160 to 580 km offshore, balances a portion of the DWBC transport [*Bryden et al*., 2005a]. The Antilles Current in the shallow 1000 m water, which has a maximum northward velocity of 40 cm s^{-1}, is adjacent to the boundary and is compensated by an offshore shallow southward current. Wb5 is located on the Hatteras Abyssal Plain (Figure 2) which extends to 35°N [*Richman et al*., 1977]

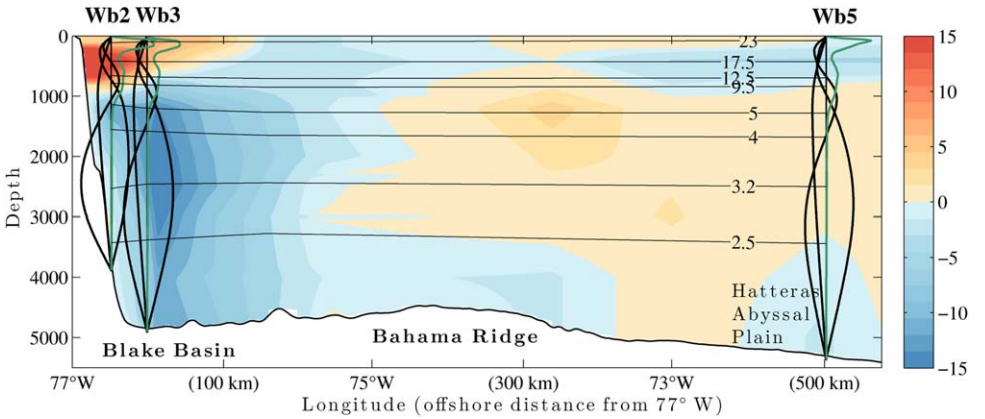

Figure 2. Bathymetry of the western boundary from ETOPO1 with the mean velocity (colors) from current meter arrays between 1986 and 1997 as described in *Bryden et al*. [2005a] and mean isotherms (black lines) from the RAPID array between 2004 and 2011. The three moorings of the boundary array Wb2, Wb3, and Wb5 are indicated with their mean buoyancy frequency profiles (green) and the modal structure of the first three baroclinic modes of isopycnal displacements (black).

and is approximately 5300 m deep. Wb2 is situated on the continental slope of the Bahamas escarpment and Wb3 is in the Blake Basin. The Bahama Ridge is present between the Abyssal Plain and the Blake Basin; the Ridge shallows to approximately 4500 m and Wb4 is located on the western section of the Ridge.

2.2. Calculating Meridional Overturning Circulation

According to the RAPID methodology detailed in *Rayner et al*. [2011], the MOC is defined as the northward transport which is integrated from the surface to the level of maximum transport. This level occurs around 1100 dbar at the base of the permanent thermocline. The northward MOC transport arises from the sum of the Gulf Stream (T_{GS}), the Ekman (T_{EK}), and the upper mid-ocean transport (T_{UMO}). The Gulf Stream transport is measured by a telephone cable in the 800 m deep Florida Strait between the Bahamas and the coast of Florida [*Baringer and Larsen*, 2001]. The Ekman transport is obtained from zonal wind stress which comes from the Cross-Calibrated Multi Platform (CCMP) wind product. The upper mid-ocean transport, integrated from the surface to the depth of maximum transport (z_{max}) around 1100 dbar, is composed of the internal transport (T_{INT}), the western boundary wedge transport (T_{WBW}), and the external transport (T_{EXT}).

The internal transport (T_{INT})

$$T_{INT}(p,t)=\int_{x_E}^{x_W} v_{geo}(p,t)dx \tag{2}$$

is the zonally integrated geostrophic velocity (v_{geo})

$$v_{geo}(p,t)=\frac{1}{f(x_W-x_E)}\int_{p_{ref}}^{p}(\delta_W(p',t)-\delta_E(p',t))dp' \tag{3}$$

between the eastern boundary (E) and Wb2 at the western boundary (W), with f the Coriolis parameter, x the horizontal distance, δ the specific volume anomaly, and p_{ref} the reference pressure at 4820 dbar.

The western boundary wedge (T_{WBW}) is measured directly by current meters between the Bahamas and Wb2. The external transport (T_{EXT}) is a depth-independent flow that is computed at each time step in order to conserve mass transport across the section

$$\int_{p_{bottom}}^{0}(T_{GS}(p,t)+T_{EK}(p,t)+T_{INT}(p,t)+T_{EXT}(p,t)+T_{WBW}(p,t))dp=0. \tag{4}$$

The external transport is distributed uniformly over the area of the section and its profile of transport per unit depth is proportional to the zonal width of the basin at each depth. The vertical profile of T_{EXT} is almost uniform in the top 4000 dbar and decreases to zero below 4000 dbar because the longitudinal extent is not

greatly affected by the sloping boundaries or by the presence of the Mid-Atlantic Ridge (MAR). Applying the mass conservation, the upper mid-ocean transport (T_{UMO}) can be calculated

$$T_{UMO}(t)=\int_{z_{max}}^{0}(T_{INT}(p,t)+T_{EXT}(p,t)+T_{WBW}(p,t))dp. \tag{5}$$

2.3. Modal Decomposition and Spectral Analysis

A normal mode decomposition [*Gill*, 1982] is applied to analyze the vertical structure of fluctuations near the western boundary. Isopycnal displacements $\zeta(z,t)$ are decomposed into modal amplitudes $\hat{\zeta}(t)$ for M vertical modes $F_m(z)$ with $M=20$ as

$$\zeta(z,t)=\sum_{m=1}^{M}\hat{\zeta}_m(t)F_m(z), \tag{6}$$

where the modal structures are determined from

$$\frac{d^2F_m(z)}{dz^2}+\frac{N^2(z)}{c_m^2}F_m(z)=0. \tag{7}$$

The eigenvalue c_m is the phase speed of the mode-m gravity waves. The eigenvalue is associated with the eigenfunction (normal mode) F_m and N is the buoyancy frequency. Using the rigid lid approximation and assuming a flat bottomed and motionless ocean, the boundary conditions are $F(z)=0$ at $z=0$ and $z=-H$. Time series of modal amplitudes are obtained from the orthonormality condition applied to the decomposition [*Gill*, 1982].

The buoyancy frequency profile is calculated at each mooring from the time-averaged density profile derived from moored T/S measurements

$$N(z)^2=-\frac{g}{\rho_0}\frac{\partial\bar{\rho}(z)}{\partial z}, \tag{8}$$

where ρ_0 is a reference density and the overbar indicates time mean. The mean buoyancy frequency profile is calculated from March 2004 to January 2011 and displayed for each mooring in Figure 2, along with the first three baroclinic modes. Once the isopycnal displacements are determined, the density fluctuations for each mode are given by

$$\rho_m(z,t)=\bar{\rho}(z)-\hat{\zeta_m}(t)F_m(z)\frac{\partial\bar{\gamma}^n(z)}{\partial z}, \tag{9}$$

and the resulting dynamic height fluctuations of each mode and their contribution to the MOC can be determined using equations (2) and (3).

A frequency spectrum of isopycnal displacements is calculated for various baroclinic modes. Spectra are calculated using Welch's overlapped segment averaging (WOSA) method [*Emery and Thomson*, 2001]. Time series are segmented in 2 year blocks and weighted by a Hanning window with 67% overlap [*Antoni and Schoukens*, 2009]. An equivalent degree of freedom of 14 is obtained for modal amplitudes of Wb2, Wb3, and Wb5 from the percentage of overlap and the window type as defined in *Percival and Walden* [1993]. A 2-D frequency/zonal wave number spectrum of SSHA is obtained at 26.5°N also using the WOSA method. To focus on the signal of interest with the strongest effect on the SSHA variance, the spectrum is displayed in a variance-preserving form. Coherences are calculated between adjacent moorings to study the relationship at specific frequencies of modal amplitudes and SSHA. The 95% confidence interval is estimated from the equivalent degree of freedom [*Emery and Thomson*, 2001].

The Rossby wave dispersion relation is obtained from linearized quasigeostrophic equations with flat bottom, no mean flow, and continuous stratification as in *Gill* [1982]

$$\omega_m=-\frac{\beta k}{k^2+l^2+\lambda_m^{-2}}, \tag{10}$$

where ω is the wave frequency, k and l the zonal and meridional wave numbers, m the mode number, and β the meridional gradient of the Coriolis parameter. The internal Rossby radius of deformation ($\lambda_m=c_m/f$) of

each baroclinic mode is defined using the eigenvalue of equation (7). The Rossby radius at Wb5 (with $\lambda_1 =$ 47 km), which is more representative of the western basin than Wb2 and Wb3 located in boundary-intensified currents, is used in the dispersion relations of the 2-D spectrum. For long Rossby waves, the phase speed of each baroclinic mode is $c_m = -\beta\lambda_m^2$. The maximum long-wave frequency or cutoff frequency obtained for each baroclinic mode is $\omega_{m\_max} = -\beta\lambda_m/2$ assuming long meridional waves and zonal wavelength of $k_{m\_max} = \lambda_m^{-1}$. The cutoff frequency separates the nondispersive waves below ω_{m_max} from dispersive waves at higher frequencies.

2.4. Propagation From Altimetric Sea Surface Height

Sea surface height anomalies (SSHA) are produced by the Ssalto/Duacs multialtimeter system [*Ducet et al*., 2000] available from the Aviso website (CNES) and are used for the period from October 1992 to January 2011. The "reference" delayed-time product has a 7 day temporal resolution with data projected on a $1/3°$ Mercator grid. Following *Kanzow et al*. [2009], a seasonal cycle was removed from the SSHA at each longitude along 26.5°N by subtracting the zonal mean of SSHA between 77°W and 14°W at each time step. This removes an approximate steric seasonal cycle from each longitude but leaves propagating or longitudinally-dependent SSH anomalies on seasonal time scales intact. SSHA is linearly interpolated onto the location of each mooring.

A methodology based on the lagged SSHA cross correlation of *Fu* [2006] is implemented to describe the mean propagation speed and direction of SSHA in the North Atlantic from March 2004 to January 2011. SSHA time series of the center of a 300 km diameter circle are lag-correlated with SSHA of each point within the circle with a maximum lag of 100 days. The maximum correlations are retained for each point if significant at 95% confidence levels. A speed is determined from the time lag of the maximum correlations, and a direction from the position of each point relative to the circle center. A mean speed and direction (arrow length and orientation in Figure 1) is attributed to the center by averaging all the neighboring values weighted by the maximum correlations. Significant levels of the correlation coefficient are determined at 95% confidence level from a test using Student's t-distribution given the degree of freedom [*Emery and Thomson*, 2001]. The effective degree of freedom is calculated from the number of measurements over the integral timescale defined as the integrated autocovariance function to the first zero crossing.

3. Characteristics of Westward Propagating Features

3.1. Frequency and Zonal Wave Number From SSHA

The global coverage of altimetry is first used to detect the presence and location of westward propagating anomalies in the North Atlantic (Figure 1). In the absence of strong mean flow, eddies and Rossby waves are expected to propagate to the west due to the latitudinal gradient of Earth's rotation. Three main regions emerge from Figure 1 at different latitudes: the first in the subtropics equatorward of 20°N, the second at midlatitudes between 20 and 30°N, and the third from 30 to 40°N. The subtropics are characterized over the entire basin by relatively fast westward propagating anomalies which are slightly deflected northwestward when approaching the western boundary. This deflection comes mostly from the North Brazil Current orientated to the northwest along the South American coast and which creates rings that travel to the Lesser Antilles [*Fratantoni and Richardson*, 2006]. In the midlatitudes, westward propagating signals are observed across the full Atlantic basin extending to the western mooring array without being deflected at the boundary. The Gulf Stream is restricted in these latitudes to the Florida Straits and propagating anomalies are dominantly westward toward Wb5-Wb2. The phase speed dependence on β (beta effect) and on the Rossby radius from linear Rossby wave theory is apparent in the slower speeds at midlatitudes compared to the subtropics. In the latitudinal band from 30 to 40°N, the eastern basin is characterized by undefined direction of propagations particularly on the eastern side of the MAR. The influence of the Gulf Stream characterized by the region of maximal surface kinetic energy [*Brachet et al*., 2004] is seen in the western basin with faster speeds but highly variable directions, in comparison to the eastern basin and to midlatitude regions at similar longitudes. As a result, the boundary between 20 and 30°N is especially relevant when studying the evolution and demise of westward propagating signals that may affect the meridional circulation.

Having detected the presence of dominantly westward propagating signals at midlatitudes, we now focus on 26.5°N. SSHAs are displayed in a Hovmoller plot with DHA overlaid from the four moorings Wb2, Wb3,

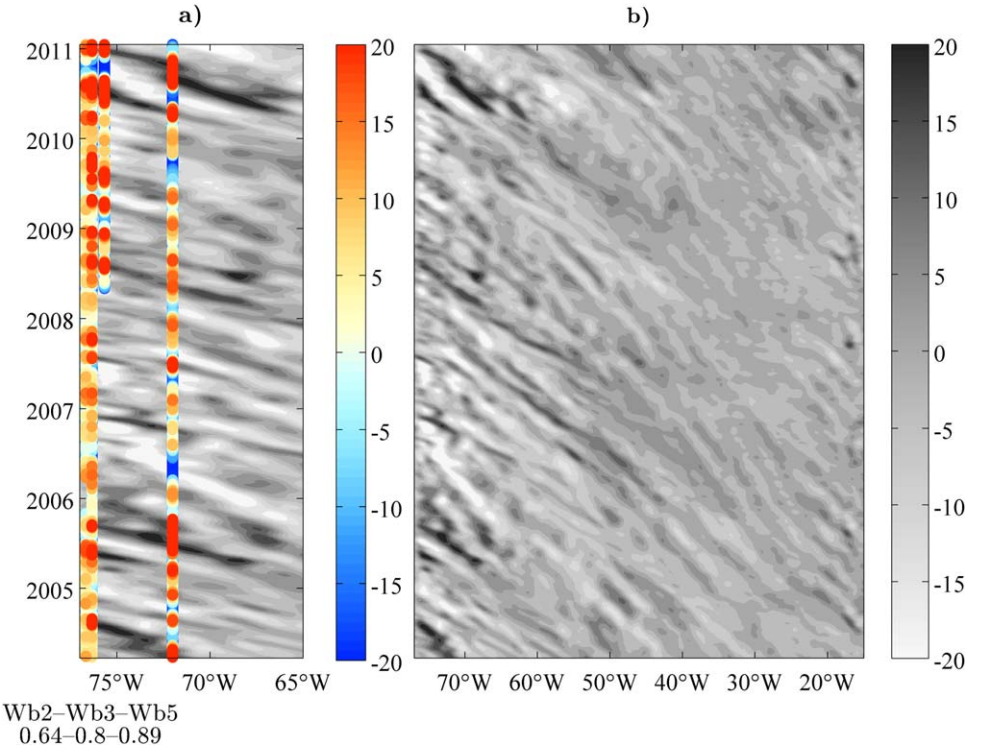

Figure 3. Dynamic height integrated from the bottom to 140 dbar (colors, dynamic cm) and sea surface height (gray, cm) anomalies at 26.5°N for (a) the westernmost section (77 to 65°W) with the four moorings of the western boundary array Wb2, Wb3, Wb4, and Wb5; (b) the entire North Atlantic basin (77 to 14°W). The correlation between DHA and SSHA is indicated below Wb2, Wb3, and Wb5.

Wb4, and Wb5 (Figure 3). High perturbations of SSHA are found at the eastern boundary and propagate to the west. However, the highest amplitudes of the eastern basin are restricted to the eastern boundary. Overall the western basin contains larger SSHA amplitudes and faster speeds of propagating signals than the eastern basin. The MAR separates the two basins at 40–50°W. A second increase in variability is visible around 65°W, before the SSHAs are dampened by the boundary at 75°W. Steric height and SSHA are known to have a strong relationship [*Gill and Niiler*, 1973], providing a link between the surface and interior signals. The correlations of SSHA with DHA significant at 95% are 0.89, 0.8, and 0.64 at Wb5, Wb3, and Wb2, respectively (Figure 3a). The decreased correlation indicates that signals at the surface are less coherent with subsurface integrated signals at Wb2 than at Wb5. While weaker, the correlation between SSHA and DHA is still significant at Wb2, supporting the hypothesis that a meridional flow inferred from geostrophic calculations could be affected by eddies and Rossby waves.

Using a 2-D (frequency-zonal wave number) spectrum of SSHA (Figure 4) and the dispersion relation of Rossby waves (equation (10)), we determine the propagation characteristics of the observed anomalies. To visualize the peak in each dimension separately, the variance integrated over zonal wave number or over frequency are also displayed. A main peak of energy appears with wavelengths in the range 350–800 km and with periods of 80–200 days. A phase speed range is inferred from these wavelengths and periods of 4.6 cm s^{-1} for the long period and long-wavelength limit of the main peak and 5.1 cm s^{-1} for the short period and small wavelength limit. Most of the peak is located above the dispersion relation of the first baroclinic mode, and these features propagate faster than predicted by the linear theory of the first mode. The energy located in the lowest frequency and lowest wave number of the peak indicates a phase speed in agreement with the dispersion relation of the first baroclinic mode Rossby wave. At the cutoff identified earlier, i.e., below the cutoff period ($2\pi/\omega_{1\_max}$ = 151 days) and wavelength ($2\pi\times\lambda_{1\_max}$ = 295 km), the dispersion relation is nondispersive. Since the ridge of energy extends to the barotropic dispersion relation for high-frequency and large wave number, this dispersive part of the spectrum may represent coupled baroclinic and barotropic motions. The phase speed discrepancy between SSHA and the linear theory was observed at midlatitudes since *Chelton and Schlax* [1996]. This observation led to the development of extended theories which included mean currents

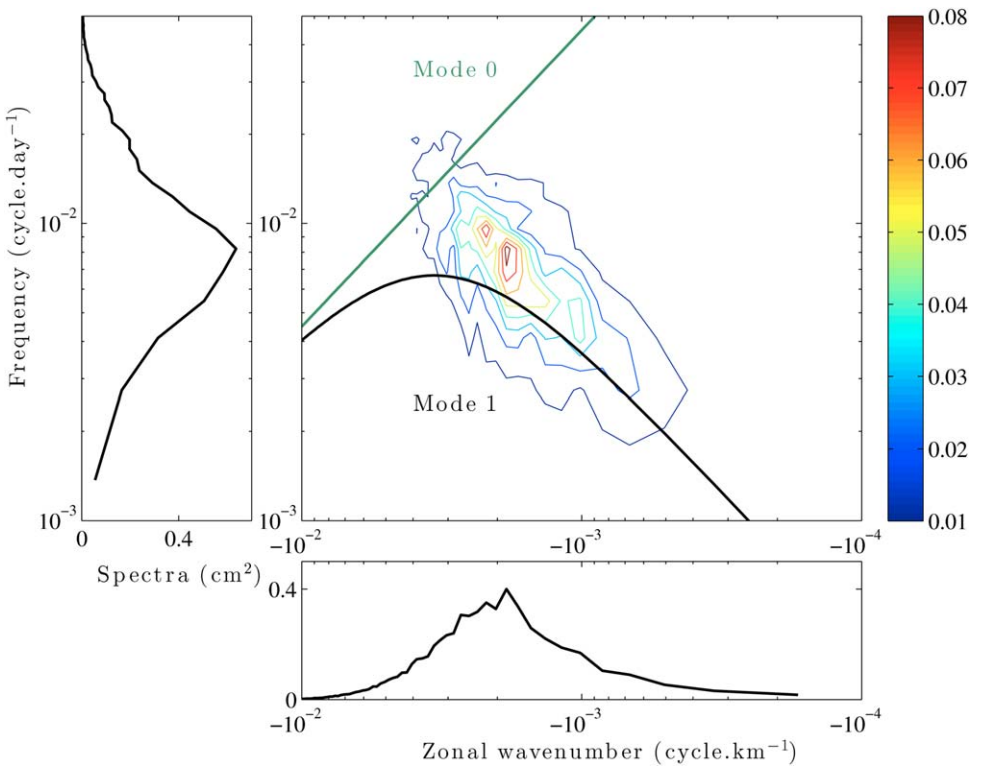

Figure 4. Frequency-zonal wave number variance-preserving spectrum (middle) of sea surface height anomaly (cm^2) in the western North Atlantic basin (77 to 18°W) at 26.5°N from October 1992 to January 2011. The dispersion relations of the barotropic and first baroclinic modes based on the linear theory are added (equation (10) with l = 0). The 2-D spectrum is shown integrated over zonal wave number (bottom) and frequency (left).

[*Killworth et al.*, 1997] and topography [*Tailleux and McWilliams*, 2000]. Subsequently, *Early et al.* [2011] favor the presence of nonlinear eddies over linear Rossby waves to represent the nondispersive part of the spectrum. Despite the agreement of the peak with the linear theory in the dispersive part of the spectrum, our observations may correspond to a nonlinear eddy regime.

3.2. Link Between Surface and Subsurface Variability

The depth to which sea surface variations are representative of the subsurface variability can be localized through the correlation coefficient of isopycnal displacements and SSHA (Figure 5). Confidence limits are calculated based on the effective degrees of freedom, inferred from the integral timescales, for SSHA and isopycnal displacements at each depth. At Wb5, the correlation is significant from the surface to 4700 m using the most conservative integral timescale of SSHA (52 days) and isopycnal displacements (30–55 days). The correlation at Wb5 varies around 0.7–0.9 in the top 1000 m and decreases below 1000 m. At Wb3 and Wb2, the correlation is still significant above 1000 m but is lower than at Wb5 with values of 0.6 and 0.5 at Wb3 and Wb2, respectively. The correlation decreases below 1000 m at Wb3 and becomes lower than the significance level around 3000 m. At Wb2, the decrease is more abrupt and the significance threshold is crossed around 1200 m. These low correlations in deep waters at Wb3 and especially at Wb2 characterize density anomalies coherent in the bottommost 2500 m which are observed in time series (not shown). These deep anomalies at the boundary are associated with the smallest integral timescales observed through the lowest significance level of the three moorings. The significance levels are almost uniform in the top 1200 m of the three moorings; the level decreases gradually at Wb5 below 1200 m as opposed to a steep decrease at Wb2. These results show that at Wb5 isopycnal displacements are more coherent throughout the water column than at the western boundary. At Wb2 and Wb3, on the other hand, the anomalies are coherent above about 1000 m. Below this depth, additional variability is found in isopycnal displacements which is uncorrelated with SSHA.

3.3. Vertical Mode Decomposition From Moorings

Modal decomposition of isopycnal displacements allows the study of the frequency and vertical structure of variability in the moorings. This variability can then be related to that in SSHAs by comparing the

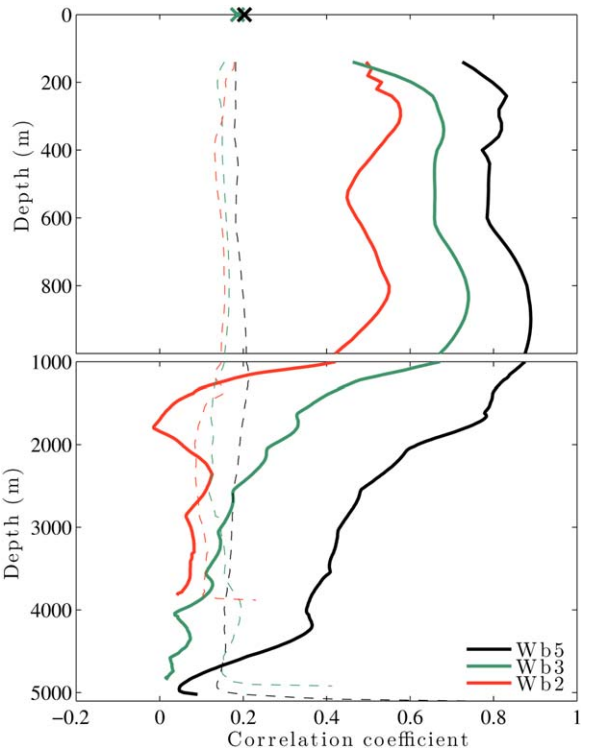

Figure 5. Correlation coefficient between SSHA and isopycnal displacements at Wb2 (red), Wb3 (green), and Wb5 (black). The 95% confidence intervals inferred from isopycnal displacements and SSHA are indicated as dashed lines and crosses, respectively.

frequencies of interest. The vertical structure is linked to horizontal propagation through the mooring array with a coherence spectra from which phase speeds and propagation directions are inferred. The effect of eddies and Rossby waves on the geostrophic transport is evaluated once an efficient representation of their vertical structure is established.

3.3.1. Eigenfunction Structure

Profiles of mean buoyancy frequency and isotherms at the western boundary are displayed in Figure 2. They are characteristic of the western North Atlantic with two peaks of strong stratification in the seasonal and main pycnocline [*Siegel et al*., 1999]. The shallow peak (around 200 m) and the deeper peak (500–1000 m) have buoyancy frequencies of 0.008 and 0.005 s^{-1}, respectively. The deeper peak is shallower at the boundary and its extent reduces to 500–900 m. The isopycnals around these depths also shoal as they approach the boundary from about 70°W. A stratification minimum at 300–400 m indicates the presence of 18°C water occurring throughout the western subtropical region.

Eigenfunctions which are obtained from the Sturm-Liouville equation (equation (7)) and the boundary conditions are displayed in Figure 2 for the first three baroclinic modes at Wb2, Wb3, and Wb5. The depth of the deep zero crossing of the third mode and of the maximum amplitude of the first mode varies between locations. The depth of the first mode maximum ranges from 980 m at Wb2 to 1120 m at Wb3 and 1240 m at Wb5. The main factors influencing the depth of the maximum is the amplification of the shallower peak of the buoyancy frequency and the 1000 m change in water depth between Wb2 and Wb3. The mode structure changes from a sinusoidal profile, found with a constant stratification, when the shallow peak of stratification intensifies. The depth of the deep zero crossing of the third mode, 1060, 1460, and 1660 m for Wb2, Wb3, and Wb5, also becomes shallower closer to the coast.

3.3.2. Modal Amplitudes of Isopycnal Displacements

The percentage of variance explained by each mode is calculated using Parseval's theorem as in *Kundu et al*. [1975]. The variance for each mode is derived by taking the depth integral of the square of buoyancy frequency times ζ (equation (6)) and applying the orthonormality condition to obtain

$$\int_{-H}^{0} N^2(z)\zeta^2(z,t)dz = \sum_{m=1}^{M} \hat{\zeta_m}^2(t). \tag{11}$$

This equation provides the instantaneous depth-integrated total energy as the sum of the contribution of each mode. The available potential energy per unit area is obtained from the right-hand side of equation (11) multiplied by half the mean density. Equation (11) is derived from the orthonormality property at each time step and does not necessarily hold over the time series. Modal amplitudes might be correlated in time between each other because phase locking can exist between various modes [*Wunsch*, 1997]. Some features might be present in adjacent normal modes at one mooring and a coherence study of modal

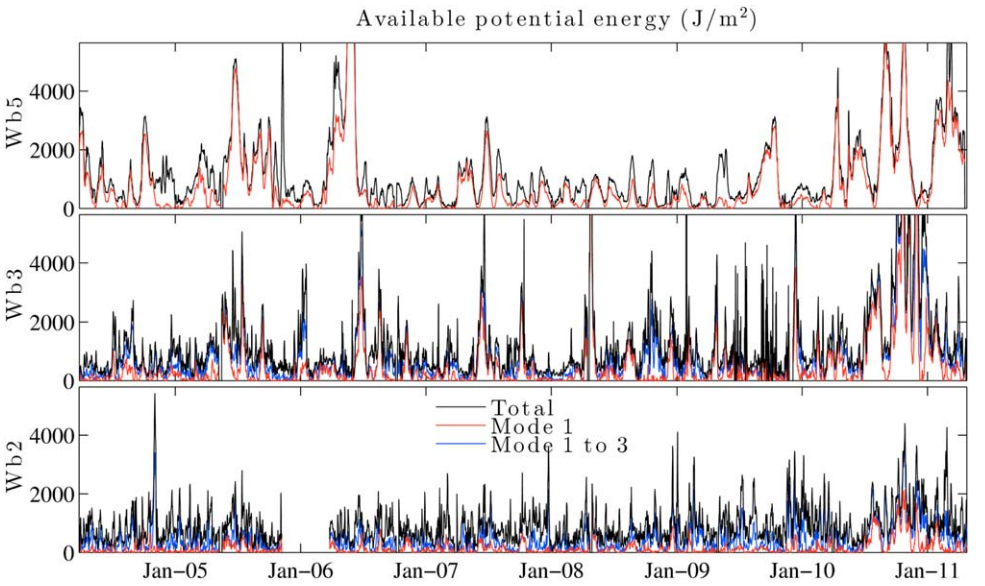

Figure 6. Available potential energy per unit area (J/m^2) at Wb5, Wb3, and Wb2 of the observed isopycnal displacements (black), the first baroclinic mode (red), and the first three baroclinic modes (blue).

amplitudes between neighboring moorings in section 3.4 will detect where true propagating signals are believed to happen. The level of available potential energy of each mooring is displayed in Figure 6. At Wb5 and Wb3, similar energy averages are noticed (1214 and 1205 J/m^2) which are larger than at Wb2 (891 J/m^2). In spite of the varying energy averages at Wb3 and Wb2, these two moorings contain a strong high-frequency variability not observed at Wb5 as found in *Szuts et al*. [2012].

The first mode at Wb5 recovers most of the energy with 52% of the variance explained, which is defined as the average of equation (11). The mode 1 and total energy are affected by processes of similar frequency. The total energy is well captured by the first mode for large events ($>$2000 J/m^2) as opposed to smaller events ($<$1000 J/m^2) for which the first mode does not represent most of the total energy. At the boundary, the first mode does not dominate and the variance explained by this mode decreases to 30% and 15% at Wb3 and Wb2, respectively. At Wb3, the events with the largest amount of potential energy are still well captured by the first mode. Events of frequency similar to the mode 1 variability at Wb3 are also seen in the first mode at Wb2 but they capture a reduced fraction of the total energy. A significant increase of the variance explained at Wb2 is provided by considering the first three modes. The variance explained by the third mode increases at the boundary with 10, 13, and 17% at Wb5, Wb3, and Wb2, respectively. The time series of the first three modes is affected by higher frequency variability than the variability of mode 1 only at Wb2. This supports our previous observation that features with the shortest integral timescales affect the deep section of Wb2 where mode 3 may be slightly dominant. A strong deep temperature anomaly below 2000 m was observed at Wb2 in November 2004 [*Cunningham et al*., 2007; *Johns et al*., 2008]. This anomaly appears at Wb2 in the total and first three modes energy but not in the first mode energy. The deep anomaly is better represented by the third mode than either the second mode (not shown) or the first mode. The percentage of variance explained by the first three modes is 45%, 60%, and 72% at Wb2, Wb3, and Wb5, respectively. Calculating the variance and the cumulative variance explained by the first 20 modes demonstrates that higher wave number variability is present at Wb2 than at Wb5. The modal decomposition with 20 modes increases the variance explained to 95% of the total energy for all moorings including Wb2.

The varying behavior of modal amplitudes throughout the array can be related to the observed link between the surface and subsurface variability. As previously noted in Figure 2, the first mode intensifies at the base of the thermocline within 200 m of 1000 m for the three moorings. This depth corresponds approximately to the depth of maximum correlation between isopycnal displacements and SSHA which has been observed increasing from the surface (Figure 5). Isopycnal displacements at each mooring are coherent within the top 1000 m, and therefore are more likely to be represented by the first mode than higher modes. In the ocean's interior at Wb5, propagating features are less likely to be influenced by the

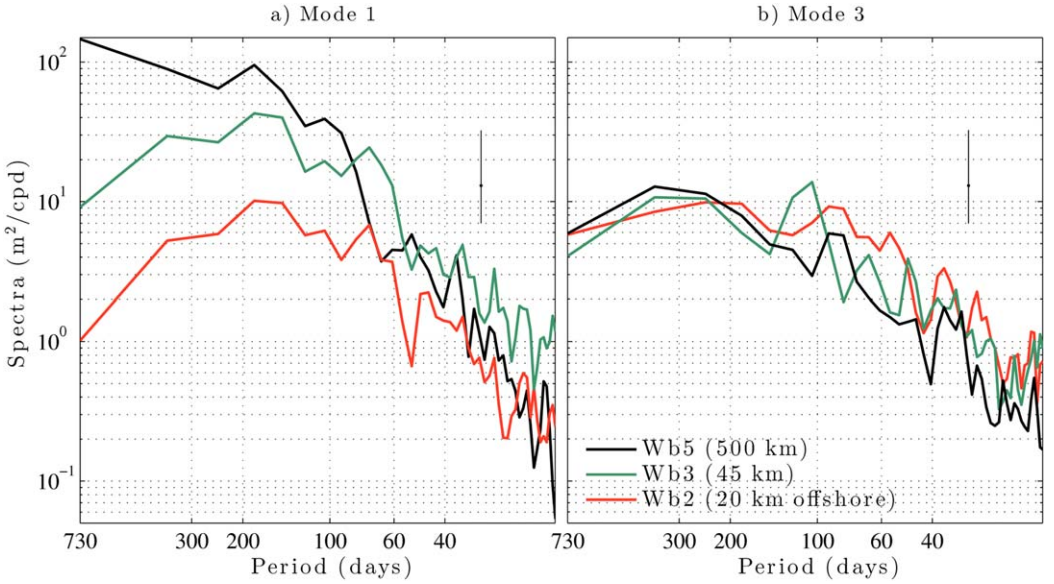

Figure 7. Power spectra of modal amplitudes of isopycnal displacement (m^2/cpd) for the first (a) and third (b) mode at Wb2 (red), Wb3 (green), and Wb5 (black) from March 2004 to January 2011. Vertical lines are the 95% confidence intervals.

topography and mean currents. The absence of these external factors may contribute to the vertical coherence of density anomalies in the full water column significantly correlated with SSHA (Figure 5) and associated with a large variance explained by the first mode (52%). At the boundary (moorings Wb2 and Wb3), the first mode still contains some energy but higher baroclinic modes are necessary to resolve the additional deep water variability represented by more complex vertical structures.

The decline of mode 1 energy in the mooring array, 500–20 km offshore, is seen in the modal amplitude spectra (Figure 7a). At Wb5, an increase in mode 1 energy is observed above 80 days which is significant at the 95% level. The spectrum is red and levels off at periods above 200 days. At Wb3 and Wb2, 45 and 20 km from the boundary, a maximum is observed around 180 days. Variability rolls off at long periods (above 200 days) at both Wb2 and Wb3. For the third mode (Figure 7b), a common period of enhanced energy is not found below 200 days in the three moorings as found for the first mode.

3.4. Propagation Between Moorings

To study propagating signals between mooring sections, we consider the coherence between SSHA and the first and third baroclinic mode signals at different locations (Figure 8). The phase is interpreted as the lag for purely westward/eastward propagating signals. High coherence indicates a high-degree of phase locking between two signals. However, coherence is normalized by the energy in the individual spectra at each frequency. As a consequence, in interpreting coherence, we focus on peaks in coherence that are also present in the individual spectra, thereby only considering a high-degree of phase locking at frequencies with large energy. As an example, between Wb3 and Wb5, coherence is enhanced at 730, 180, and 60 days. For the 180 day peak, which exhibits a peak in mode 1 variance at each mooring (Figure 7a), the phase describes westward propagating signals for both SSHA and the first baroclinic mode. In contrast, for the 730 and 60 day peaks, the spectrum at Wb3 (Figure 7a) shows little energy so we do not consider them further. The 180 day peak is coherent between 80 and 250 days but the phase is not clearly defined between 80 and 150 days. A constant phase speed of 7.3 cm s^{-1} is observed in the period range from 150 to 250 days with phases of 3 and 1.8 rad, respectively.

In the Wb2-Wb3 section, the coherence of the first mode has two major peaks with positive phase at 110–180 days and at 80 days. The 180 day peak of mode 1 has a phase speed of 4 cm s^{-1} (with a phase of 0.3 rad) at the boundary between Wb2 and Wb3 which is slower than the value observed in the interior between Wb3 and Wb5 (7.3 cm s^{-1}). Comparing this speed (7.3 cm s^{-1}) to those inferred from the 2-D spectrum of SSHA (4.6–5.1 cm s^{-1}) over the whole basin, the mooring measurements suggest that phase propagation is faster in the western basin. The phase-speed decrease at the boundary may partly be due to a

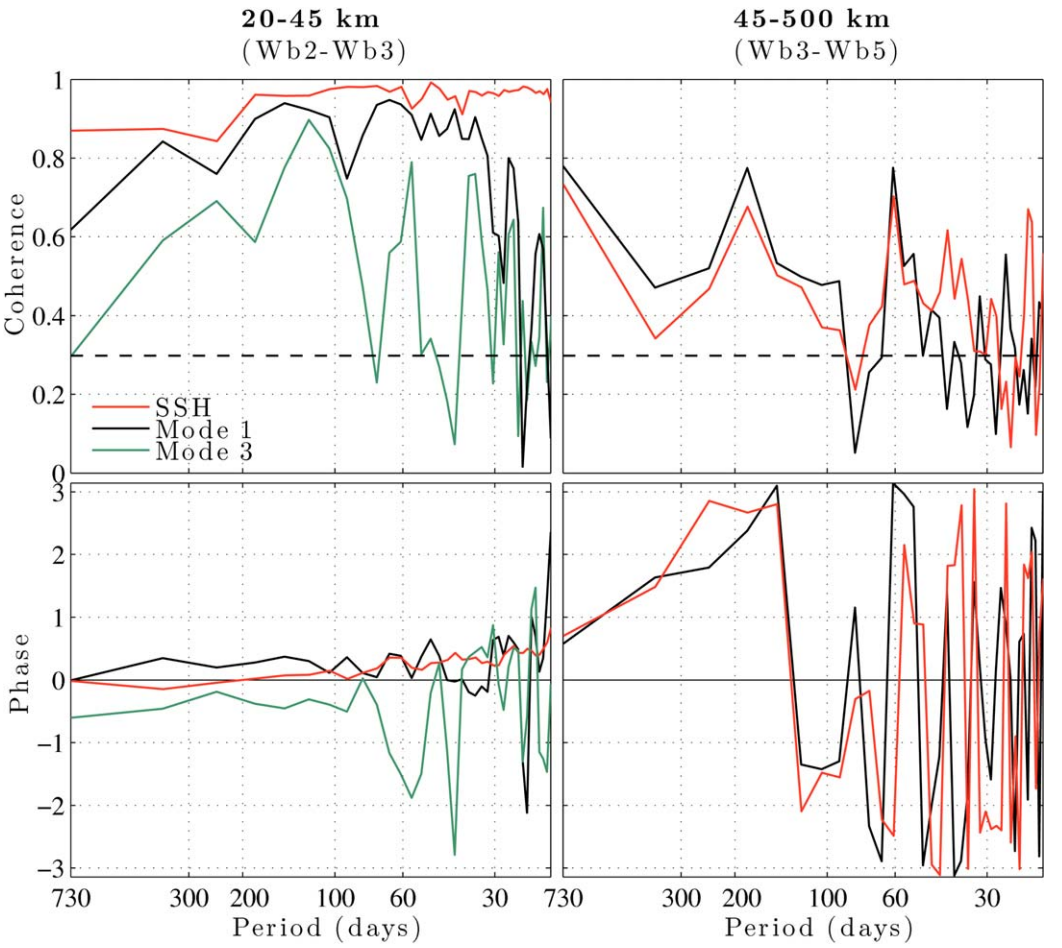

Figure 8. Coherence (top) and phase (bottom) between Wb2 and Wb3 (left) and between Wb3 and Wb5 (right) for sea surface height anomaly (red), modal amplitudes of the first baroclinic mode (black), and third baroclinic mode (green). The 95% significance level of the coherence is indicated by the black-dashed line.

blocking effect caused by the western boundary. Because the spatial resolution of the gridded SSHA altimetry product is coarser than the distance between Wb2 and Wb3, SSHA interpolated to the two mooring positions appears coherent at all periods. Coherence of the third mode between Wb2 and Wb3 has a major peak at a 120 day period with a negative phase, but no common peak of enhanced variance was observed at this frequency in both moorings (Figure 7b).

4. Effect on the Meridional Circulation

In the previous section, we identified the dominant period, zonal wavelength, and vertical structure of westward propagating features. Upon arriving at the boundary, they will either deepen or shoal the isopycnals at the thermocline, changing the incline between the eastern and western boundary. In this wave pattern, each crest and trough is associated with a positive or negative anomaly, but across a full period of crest and trough, the transport anomaly is essentially zero. The effect on the MOC is strongest when an eddy or the wave arrives at the boundary, loses its symmetry, and thus causes a net meridional transport.

4.1. Geostrophic Transport of First Mode Signals

Using the modal amplitudes and the vertical structure of the modes, we reconstruct the density profile at Wb2 associated with the modal activity (Figure 9). The observed variability is well captured above the thermocline, around 1000 m. Large vertically coherent displacements lasting several months are represented by first mode vertical structure of isopycnal displacements. Just below our minimum depth of 140 m, additional high-frequency isopycnal variability is observed and is not captured by this mode. Isopycnal displacements go to

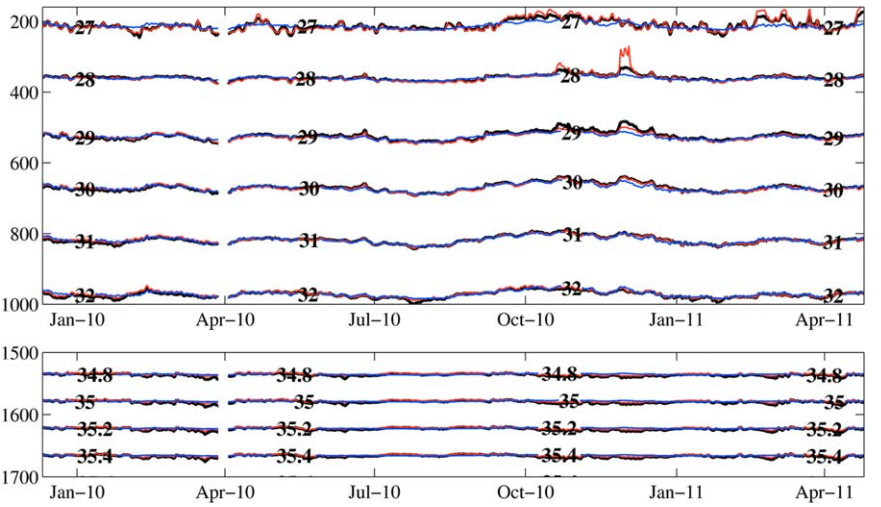

Figure 9. Observed isopycnals at Wb2 (black) and reconstructed isopycnals attributed to the first (blue) and the first 20 (red) baroclinic modes above 1000 m (top) and zoomed in the deep layer between 1500 and 1700 m (bottom). The time period shown is a subset of the entire record chosen as a representative example.

zero at the surface because of the boundary condition of the modal decomposition which means that the modes will be unable to represent any intense near-surface variability measured by the array. Other representations consider surface buoyancy anomalies using a surface quasigeostrophic mode [*Lapeyre*, 2009]. Because the RAPID moorings are not designed to measure shallow or surface hydrographic properties, surface quasigeostrophic modes cannot be accurately assessed. From the insignificant correlation of SSHA and isopycnal displacements below 1200 m at Wb2 (Figure 5), the first mode is not expected to reproduce the deep signal. The inclusion of higher baroclinic modes is necessary to recover the deep variability as seen in the agreement between isopycnals and the isopycnal variability attributed to the first 20 modes. The geostrophic velocity can be computed using the first mode contribution at the western boundary (equation (3)).

To study the eddy and Rossby wave activity at the western boundary only, the dynamic height at the eastern boundary is fixed to its temporal mean for the calculation of the geostrophic internal transport attributed to mode 1 (equation (2)). The geostrophic transport anomaly attributed to the first mode ($T'_{INT\,mode1}$) is compared to the observed transport (T'_{INT}) in Figure 10, both calculated by integrating equation (2) either above 1100 m or below 1100 m. The mode 1 variability captures a significant amount of the observed shallow transport on subannual timescales. The correlation between the two shallow transports of 0.77 is significant at 95% giving a variance explained by the first mode of 59%. The phases of the subannual variability in both transports agree but the amplitudes of the anomaly vary. The amplitude of the mode 1 transport is weaker than the amplitude of the observed transport. This is reflected in the standard deviation of 5.5 Sv for T'_{INT} being higher than 3.5 Sv for $T'_{INT\,mode1}$. Since we have shown that most of the variance of westward propagating features is recovered by a first mode vertical structure, we estimate an upper limit of the effect of eddies and Rossby waves on the geostrophic transport to be about 3.5 Sv.

Below 1100 m, the transport attributed to mode 1 contains small variations (standard deviation of 0.4 Sv) which are an order of magnitude smaller than the variability of the observed transport (5.1 Sv); both transports are not significantly correlated. This is expected from the increased importance of higher baroclinic modes that represent the deep boundary variability as seen in the insignificant correlation between isopycnal displacements and SSHA below 1200 m at Wb2 (Figure 5).

The influence of westward propagating features on interannual timescales is evaluated by comparing 1 year low-pass filtered transports ($T'^{t>1year}_{INT}$ versus $T'^{t>1year}_{INT\,mode1}$) in Figure 10. Mode 1 has weaker interannual variability, with a standard deviation of 0.6 Sv. In contrast, the observed transport has larger anomalies on interannual timescales, with a standard deviation of 2.4 Sv. The weaker correlation (0.41), which is obtained for interannual timescales only, supports the reduced effect of westward propagating features on interannual transports. This correlation is not significantly different than zero because of the reduced degrees of freedom of low-passed filtered transports. Weaker interannual variability in the reconstructed transport is

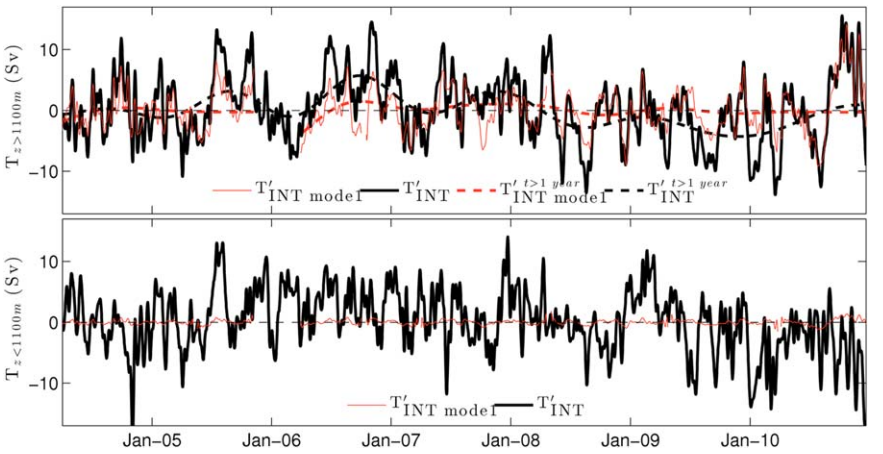

Figure 10. Geostrophic meridional transport anomaly observed (T'_{INT}, black line) and attributed to the first baroclinic mode ($T'_{INT\,mode1}$, red line) at the western boundary for the upper 1100 m (top) and below 1100 m (bottom). The correlation coefficient between the observed (T'_{INT}) and first mode ($T'_{INT\,mode1}$) internal transports is 0.77 in the upper layer and 0.09 in the deep layer. The dashed lines indicate the interannual (1 year low-pass filtered) observed upper transport ($T'^{t>1year}_{INT}$) and upper transport attributed to mode 1 ($T'^{t>1year}_{INT\,mode1}$). The correlation between the two low-pass filtered upper transports is 0.41.

anticipated by the frequency spectrum of the mode 1 amplitudes at Wb2 (Figure 7a) with low variability at interannual timescales. The reduction was observed for periods of 250–730 days based on the choice of 2 year block averaging. To conclude, mode 1 variations associated with Rossby waves and eddies do not appear to affect the geostrophic transport on interannual timescales. From the low frequency limit used in the block averaging, we cannot rule out the effect of large-scale Rossby waves with periods larger than 2 years or of a nonstationary eddy regime at midlatitudes.

4.2. Effect of Westward Propagating Processes on the Upper Mid-Ocean Transport

To study the effect of mode 1 propagating anomalies, the variability added by these processes is first analyzed in the transbasin geostrophic velocity profile. Then the barotropic compensation is presented. The profile of mean meridional geostrophic velocity is shown in Figure 11. The velocity contains a maximum around 900 m surrounded by a local minimum between 1600 and 2000 m and a strong decrease above 900 m. The standard deviation of the velocity is added to compare the variability of the observed velocity against the variability of the velocity due to mode 1. The standard deviation of the observed velocity is larger than 0.05 cm s^{-1} above 1100 m and larger than 0.02 cm s^{-1} above 3500 m. The standard deviation of the velocity attributed to mode 1 is two times smaller than the observed velocity above 1000 m with a value of 0.02 cm s^{-1} and is strongly reduced below 1500 m ($<5\times10^{-3}$ cm s^{-1}). The vertical extent in the top 1000 m of the large standard deviation attributed to mode 1 is expected from the mode 1 structure and also from the presence of higher baroclinic modes at the boundary.

The effect of eddies and Rossby waves on the upper mid-ocean transport (T_{UMO}), directly related to the MOC, can now be established. T_{UMO} is obtained by applying a barotropic adjustment (T_{EXT}) that conserves mass transport (equation (4)) to the geostrophic internal transport (T_{INT}). The compensation, which depends on the Gulf Stream, Ekman, wedge, and internal transports, is uniformly distributed over the area of the cross section. The variability attributed to first mode features in T_{INT} is similarly redistributed at each depth. The compensating process of eddy and Rossby wave signatures in T_{INT} was believed to explain part of the significant correlation observed between the internal and external transports in *Kanzow et al.* [2007]. Knowing the longitude, where geostrophic transport anomalies are created, may indicate the location where the barotropic adjustment is most likely to take place in the section.

To isolate the effect of mode 1 anomalies on the upper mid-ocean transport, the Gulf Stream, Ekman, wedge transports, and eastern boundary density are fixed to their temporal mean in $T_{UMO\ mode1}$. This transport is compared to the observed T_{UMO} (Figure 12) and a significant correlation of 0.65 is found between the two transports. A reduction in the correlation between the observed transport and mode 1 transport is expected when moving from T_{INT} to T_{UMO} because the wedge and external transports add additional variability (equation (5)). The slight reduction of correlation from 0.77 to 0.65 indicates that the effect of eddies

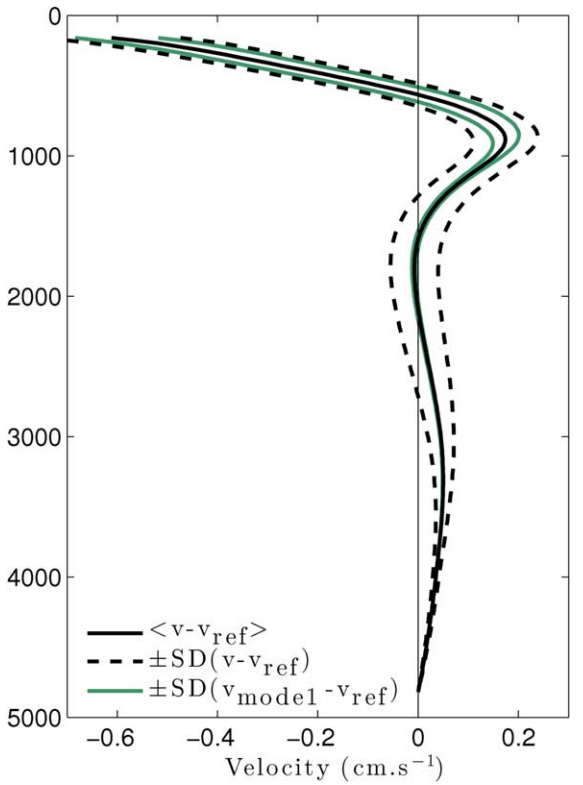

Figure 11. Mean (black) and mean ± the standard deviation (dash black) of the geostrophic meridional velocity between the western and eastern boundary. Mean ± the standard deviation of the geostrophic meridional velocity using mode 1 density profile at the western and a mean density profile at the eastern boundary (green).

and Rossby waves is still large and explains 42% of the variance of T_{UMO}. As noted for T_{INT}, the amplitude of T_{UMO} variability attributed to mode 1 (2.6 Sv) is smaller than observed (3.4 Sv).

Mode 1 features have little effect on the geostrophic transport below 1100 m (Figures 10 and 11). The external transport, however, redistributes the variability of $T_{INT\,mode1}$ and projects onto the upper North Atlantic Deep Water (UNADW, 1100–3000 m) and lower North Atlantic Deep Water (LNADW, 3000–5000 m) layers (not shown). UNADW and LNADW are composed of the internal, external, and wedge transports. The external transport variability in the deeper layers is roughly twice the magnitude as that in the upper mid-ocean layer, since the layers are twice as thick. In these two deep layers, however, mode 1 does not significantly contribute to their variance, as indicated by the small correlations between mode 1 transport and the upper layer (0.06) or the lower layer (0.23).

To link the mode 1 variability to the MOC, we compare the upper geostrophic transport attributed to mode 1 ($T_{UMO\ mode1}$) and the observed MOC where Ekman is held constant. Ekman transport is fixed in order to isolate the geostrophic components of the MOC from the direct wind effects. A significant correlation of 0.30 is found, explaining 9% of the variance. This result underlines the importance of localized eddies and Rossby waves in explaining some of the subannual variability of the MOC as opposed to longer timescales processes such as deep water formation rates.

4.3. Meridional Extent of Subannual Transport Anomalies

The question arises as to what extent subannual variations of the MOC are meridionally coherent. From the zonal RAPID array, we cannot directly estimate meridional coherence. However, we have shown that the dynamic height at Wb2 shows a high correlation (0.64) with nearby SSHA, while the mode 1 amplitude at Wb2 correlates slightly better (0.67) with SSHA. Using the reconstruction of the interior transport from the first mode (first three modes) with correlations of 0.77 (0.81) with the observed interior transport, we see that mode 1 fluctuations are the primary driver of meridional transport variability. This suggests that sea surface height variability can be used to explain some meridional transport variability along the western boundary of the Atlantic. By calculating the meridional coherence of sea surface height variations extracted along the 3900 m isobath (results not shown), we find that the sea surface height quickly becomes decorrelated with latitude. At three degrees north or south, the correlation reduces to 0.2, the level of statistical difference from zero at 95% confidence. The meridional scale (600 km) obtained from the north and south decorrelation scales is consistent with the zonal wavelength of 350–800 km of the 2-D SSHA spectrum assuming isotropic eddies.

5. Discussion

5.1. Eddy and Rossby Wave Characteristics

Westward propagating signals with periods of 80–250 days have been identified near the western boundary from altimetry and in situ moorings. The offshore mooring (Wb5) additionally indicates that the energy is in

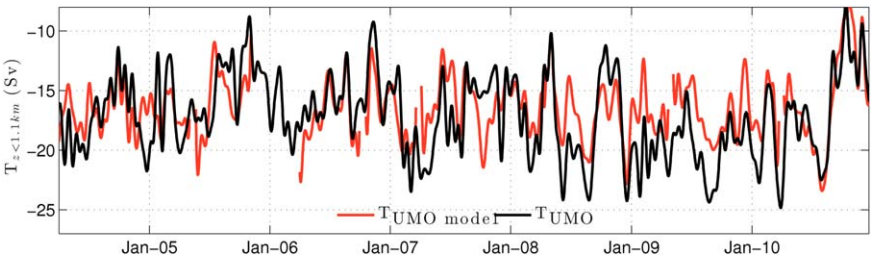

Figure 12. Upper mid-ocean transport observed (T_{UMO}, black) and reconstructed with the first baroclinic mode at the western boundary ($T_{UMO\ mode1}$, red). The correlation between the two transports is 0.65.

the first baroclinic mode, with translational speeds (7.3 cm s^{-1}) higher than the speed found over the basin (4.6–5.1 cm s^{-1}) from the 2-D SSHA spectrum. Both speeds are higher than those predicted by the linear Rossby wave dispersion relation ($\beta\lambda_1^2$=4.5 cm s^{-1}). Using sea surface temperatures, *Halliwell et al.* [1991] identified a similar peak with a period of 200 days in the North Atlantic Subtropical Convergence zone (59.5–75.5°W and 22.5–33.5°N). *Osychny and Cornillon* [2004] used zonal wave number/frequency spectra of SSHA, and identified two peaks: a 180 day peak observed primarily in the latitude band of 25–41°N, and a 700 day peak which was present equatorward of 25°N. This latitude, where the RAPID array is located, has been described as a transition region between a linear Rossby wave-dominated region equatorward, and a turbulent regime of nonlinear eddies poleward of 25°N [*Chelton et al.*, 2007; *Tulloch et al.*, 2009] with higher phase speeds than predicted by the linear Rossby wave theory. The peak found in our study at periods of 80–250 days and observed northward of the array [*Halliwell et al.*, 1991; *Osychny and Cornillon*, 2004] may be more characteristic of an eddy regime.

Having detected a region of mostly westward propagating features at midlatitudes from altimetry, the observed variability of SSHA was associated with the first baroclinic mode. This result was expected from the significant correlation of SSHA with DHA and the observation that DHA mainly represented the first mode [*Siegel et al.*, 1999]. *Stammer* [1997] previously linked the first mode and surface variability by correlating SSH eddy spatial scale with the first mode Rossby radius. This result was confirmed by *Wunsch* [1997] which related regions of elevated first mode kinetic energy measured by current meters with regions of enhanced surface kinetic energy. Both studies observed three areas of varying dynamics using SSH spectra and normal modes of velocity: regions with significant boundary currents, interior tropical regions, and interior extratropical regions. In the present study, the importance of the first mode was observed in the midlatitude interior ocean but also at the western boundary region, despite the increased importance of higher baroclinic modes. The first mode variability was enhanced for the three moorings at periods of 80–250 days. This range agrees with the period of mesoscale variability (100 days) previously detected from current meters by *Lee et al.* [1996] or in the MODE array [*Richman et al.*, 1977]. Closer to the boundary, the relative importance of the third mode increases, suggesting that this mode may be locally generated either by rough topography, interactions with the boundary, or from meridionally propagating waves.

Although we concentrated on purely westward propagating signals, the origin of these anomalies is not localized. Along the zonal RAPID array, additional variability can be added by processes originating at different latitudes. In Figure 3, enhanced variability is present at both the eastern boundary due to local wind stress curl [*Chidichimo et al.*, 2010], and west of 60°W from Gulf Stream rings [*Parker*, 1971]. In the eastern basin, eddies are created by trade winds and Canary Current anomalies and transported to 25°N before travelling westward [*Sangrà et al.*, 2009]. *Sangrà et al.* [2009] observed, however, that only 10% of these eddies are long-lived, the rest enter the background turbulence around 25°W and do not seem to contribute significantly to variability in the western basin. The speed increase observed around 40–50°W (Figure 3) may be attributable to the deepening of the thermocline [*Chelton et al.*, 1998] or to topographic interactions with the MAR [*Tailleux and McWilliams*, 2000]. There is also the potential for eddies shed from the North Brazil current to propagate northward to the RAPID latitude [*Jochumsen et al.*, 2010]. These additional sources of variability as well as atmospheric forcing over the basin interior may degrade the coherence between anomalies generated at the eastern boundary from propagating all the way to the west.

5.2. Deep Variability at the Western Boundary

In the ocean interior at Wb5, mode 1 dominates the variability with fluctuations of the same sign over the full depth and maximum amplitude in the thermocline. In contrast, at the boundary, anomalies are still present in the thermocline, but added variability appears in the less stratified region below 1200 m at Wb2. This depth is beneath the deeper zero crossing of the third mode at 1060 m, explaining the intensification of this mode by deep anomalies. The energy in the third mode may involve multiple processes and requires further study to thoroughly disentangle. The presence of rough topography was shown to increase the eddy baroclinicity [*Rhines*, 1977; *Treguier and Hua*, 1988], as opposed to the typical inverse energy cascade to larger vertical and horizontal scales of stratified oceanic simulations [*Fu and Flierl*, 1980; *Smith and Vallis*, 2001]. The rougher topography of the Bahama Ridge and Blake Basin, compared to the smoother Hatteras Abyssal Plain (Figure 2), may have contributed to the separation of the thermocline variability from that at deeper depths as found in the *MODE Group* [1978].

In addition to the effect of rough topography, the steep slope at the western boundary may support topographic waves or reflect incoming signals and a wide range of dynamical processes may account for some of the observed signals. The importance of the third mode energy at Wb2, in a region where the DWBC is blocked compared to Wb3, suggests that the continental wall is involved. Topographic Rossby waves propagating southward and excited by incoming eddies [*Louis and Smith*, 1982] may be present due to a larger topographic β-effect over planetary β. Additional meridional signals might also be detected from eddies travelling along the coast driven by the image effect [*Shi and Nof*, 1994]. Further study of nonlinear interactions [*Fu and Flierl*, 1980] may show whether the eddy energy pathway toward modes of smaller vertical wavelengths is active [*Dewar and Hogg*, 2010].

5.3. Contribution to the Meridional Transport

The question of the impact of eddies on the MOC arose from a series of prior papers on the topic. To evaluate the eddy variability on the MOC, *Wunsch* [2008] relied on the covariability of SSHA and density anomalies to link the observed SSHA rms to the dynamically significant first mode. By assuming SSHA fluctuations of 16 cm near the Bahamas, which is characteristic of the maximum values found in the western basin, *Wunsch* [2008] predicted a rms transport (16 Sv) many times larger than found in the observations (3.1 Sv, *Cunningham et al*. [2007]). *Kanzow et al*. [2009] attributed the difference between the observed variability and that predicted in *Wunsch* [2008] to the decrease of SSHA and DHA variability when approaching the boundary and estimated that at most 4.2 Sv of the transport variability could be attributed to westward propagating signals. They calculated this upper limit by extending the variability of a 2 year time series transport with the 15 year-long SSHA variability.

Although the present study also observed a decrease in variability of the first mode close to the boundary at 26.5°N, westward features are still responsible for a substantial portion of the meridional transport variability above the thermocline. The influence of these features on the meridional circulation was evaluated: 59% of the variance of the internal transport and 42% of the variance of the upper mid-ocean transport are attributed to first mode signals, with periods of 80–250 days. Given the other sources of the MOC variability, these anomalies account for 9% of the variance of the MOC with a fixed Ekman transport. The upper mid-ocean transport standard deviation attributable to mode 1 processes was found to be 2.6 Sv instead of the upper limit of 4.2 Sv found in *Kanzow et al*. [2009]. By comparing eddy-permitting and non-eddying global ocean models, *Hirschi et al*. [2013] estimated that 20–30% of the MOC variability could be attributed to the unpredictable chaotic fluctuation of eddies, Rossby and Kelvin waves in an eddy-permitting model. They expected to find a larger percentage associated with chaotic signals if they used a model that was eddy-resolving. This result needs to be compared cautiously to our findings as the percentage of MOC variability in *Hirschi et al*. [2013] is defined as the ratio of chaotic MOC over total MOC standard deviations.

The primary effect of westward propagating features was found on subannual timescales in a specified period range (80–250 days); interannual variability is less affected by mode 1 anomalies. This temporal distinction may facilitate the detection of large-scale oceanic anomalies with important climatic effect from more localized transport variability attributed to inherently chaotic ocean dynamics. In this regard, the 30% MOC decline described by *McCarthy et al*. [2012] from early 2009 to mid-2010 and observed in the Ekman, upper mid-ocean and LNADW transports does not appear to be associated with westward propagating features. This can be seen from the anomalies present in T_{UMO} but not in $T_{UMO\ mode1}$ (Figure 12). This event

was associated with a strengthening of the southward thermocline transport and a decline in the southward LNADW, neither of which were captured by the mode 1 transports as seen in Figure 12 for T_{UMO}. The temporal extent of the 2009–2010 event is longer than the period of maximum low-frequency energy (200 days) at Wb2 (Figure 7a). The longest period (250 days) that exhibits westward propagation may also help to disentangle and interpret any expected slowdown trend of the MOC, as predicted in the oceanic circulation of a changing climate with increasing greenhouse gases. The upper limit of the transport variability attributed to propagating features is 2.6 Sv. Any decadal variability or trend that may be found using extended continuous measurements as noticed in *Smeed et al*. [2014] and that is higher than the upper limit, may be distinguished from the effect of propagating anomalies. This result assumes that eddy and Rossby wave regimes do not change with time, which may not be entirely true within a changing climatic system composed of increasingly extreme events.

5.4. Interpretation in the North Atlantic Midlatitudes

Westward propagating signals affect the meridional transport when anomalies encounter the western boundary and cause a net displacement of isopycnals from their average depth. The eddies with mode 1 structure may modulate the northward Antilles Current and affect the southward DWBC as mentioned in *Lee et al*. [1996] and *Johns et al*. [2008]. For example, the presence of an anticyclone at the boundary may enhance the northward Antilles Current and shift the DWBC offshore [*Lee et al*., 1996]. This would be translated into an anticorrelation of the inshore versus offshore transports as found in *Bryden et al*. [2005a] and *Meinen et al*. [2013]. In the present study, we focus on the boundary, where the effect on the deep geostrophic transport was reduced because propagating processes have a weak signal below 1200 m. The interplay of westward propagating signals with the DWBC seems to be twofold. DWBC meanders are related to eddy events but the modal structure of anomalies may also be affected by the presence of a strong vertical shear between the Antilles Current and the DWBC. The DWBC may be partly responsible for the decrease in the vertical coherence of propagating anomalies limited to the shallowest 1200 m after they encounter it.

The present study highlights the importance of considering eddies and Rossby waves to describe the subannual variability of the MOC and confirms their effect on the overturning circulation calculated within the RAPID program. Westward propagating anomalies play a significant role in the MOC variability at the latitude of the RAPID array and may modulate divergence/convergence of the meridional transport on short timescales [*Sinha et al*., 2013]. The meridional coherence of the transport will be influenced by this variability and is found to decorrelate within three degrees of latitude. This analysis suggests that much of the subannual variability at 26.5°N will be local, as suggested by *Bingham et al*. [2007]. In addition to the role of eddies in the export of nutrients, heat and hydrographic properties, the understanding of their effect on large scale circulation and on the climate system is of major importance to the current improvement of global circulation models ranging from eddy-permitting to eddy-resolving [*Marsh et al*., 2009; *Hirschi et al*., 2013]. Further study on the interaction of westward propagating signals with the boundary may provide insight into the pathways of conversion or destruction of mesoscale energy in the ocean.

6. Conclusions

1. The presence of eddies and Rossby waves was detected with the global coverage of altimetry in the North Atlantic basin at 26.5°N. These features propagate westward with zonal wavelengths of 350–800 km and periods of 80–200 days.
2. Using a tall deep mooring array, the vertical structure of the westward propagating features at 72°W, 26.5°N is characterized. These have a first baroclinic mode structure intensified in the thermocline at periods of 80–250 days, consistent with observations from altimetry.
3. At the western boundary (between 77 and 76°W), a first baroclinic mode signal is found with a maximum also around 180 days, as well as deep variability associated with the third baroclinic mode.
4. The eddy and Rossby wave regime influences the subannual meridional transport. To evaluate the effect of propagating features at the western boundary, the meridional transport was calculated using the influence of mode 1 only. A correlation of 0.65 was found between the observed upper mid-ocean transport and the upper mid-ocean transport computed using mode 1 variations with Gulf Stream, Ekman, wedge transports, and eastern boundary density held constant.

5. The variability of the transbasin geostrophic transport attributed to eddies and Rossby waves is estimated to be 2.6 Sv.

Acknowledgments
The author would like to thank Dr. Joel J.-M. Hirschi, Prof Harry L. Bryden, and Prof Alberto C. Naveira Garabato for their helpful comments. L. Clément was supported by a NERC grant (NE/I528626/1). The RAPID-WATCH MOC monitoring project is funded by the U.K. Natural Environment Research Council, the U.S. National Science Foundation, and the U.S. National Oceanic and Atmospheric Administration. Z. B. Szuts was supported by an Abrupt Climate Change Research fellowship from the Comer Science and Education Foundation and by the Max Planck Society for the Advancement of Science. Data from the RAPID-WATCH project are available on http://www.rapid.ac.uk/rapidmoc/. The altimeter products were produced by Ssalto/Duacs and distributed by Aviso, with support from Cnes (http://www.aviso.oceanobs.com/duacs/).

References

Antoni, J., and J. Schoukens (2009), Optimal settings for measuring frequency response functions with weighted overlapped segment averaging, *IEEE Trans. Instrum. Meas.*, *58*, 3276–3287.
Baringer, M. O., and J. C. Larsen (2001), Sixteen years of Florida current transport at 27°N, *Geophys. Res. Lett.*, *28*, 3179–3182.
Bingham, R. J., C. W. Hughes, V. Roussenov, and R. G. Williams (2007), Meridional coherence of the North Atlantic meridional overturning circulation, *Geophys. Res. Lett*, *34*, L23606, doi:10.1029/2007GL031731.
Brachet, S., P. Y. Le Traon, and C. Le Provost (2004), Mesoscale variability from a high-resolution model and from altimeter data in the North Atlantic Ocean, *J. Geophys. Res.*, *109*, C12025, doi:10.1029/2004JC002360.
Broecker, W. S. (2003), Does the trigger for abrupt climate change reside in the ocean or in the atmosphere?, *Science*, *300*, 1519–1522.
Bryden, H. L., W. E. Johns, and P. M. Saunders (2005a), Deep western boundary current east of Abaco: Mean structure and transport, *J. Mar. Res.*, *63*, 35–57.
Bryden, H. L., H. R. Longworth, and S. A. Cunningham (2005b), Slowing of the Atlantic meridional overturning circulation at 25°N, *Nature*, *438*, 655–657.
Bryden, H. L., A. Mujahid, S. A. Cunningham, and T. Kanzow (2009), Adjustment of the basin-scale circulation at 26°N to variations in Gulf Stream, deep western boundary current and Ekman transports as observed by the Rapid array, *Ocean Sci.*, *5*, 421–433.
Chelton, D. B., and M. G. Schlax (1996), Global observations of oceanic Rossby waves, *Science*, *272*, 234–238.
Chelton, D. B., M. G. Schlax, K. E. Naggar, and N. Siwertz (1998), Geographical variability of the first baroclinic Rossby radius of deformation, *J. Phys. Oceanogr.*, *28*, 433–460.
Chelton, D. B., M. G. Schlax, R. M. Samelson, and R. A. de Szoeke (2007), Global observations of large oceanic eddies, *Geophys. Res. Lett.*, *34*, L15606, doi:10.1029/2007GL030812.
Chidichimo, M. P., T. Kanzow, S. A. Cunningham, W. E. Johns, and J. Marotzke (2010), The contribution of eastern-boundary density variations to the Atlantic meridional overturning circulation at 26.5°N, *Ocean Sci.*, *6*, 475–490.
Cunningham, S. A., et al. (2007), Temporal variability of the Atlantic meridional overturning circulation at 26.5°N, *Science*, *317*, 935–938.
Desaubies, Y., and M. C. Gregg (1981), Reversible and irreversible fine structure, *J. Phys. Oceanogr.*, *11*, 541–556.
Dewar, W. K., and A. M. Hogg (2010), Topographic inviscid dissipation of balanced flow, *Ocean Modell.*, *32*, 1–13.
Ducet, N., P. Y. Le Traon, and G. Reverdin (2000), Global high-resolution mapping of ocean circulation from TOPEX/Poseidon and ERS-1 and −2, *J. Geophys. Res.*, *105*, 19,477–19,498.
Early, J. J., R. M. Samelson, and D. B. Chelton (2011), The evolution and propagation of quasigeostrophic ocean eddies, *J. Phys. Oceanogr.*, *41*, 1535–1555.
Emery, W., and R. Thomson (2001), *Data Analysis Methods in Physical Oceanography*, 634 pp., Pergamon Press, Amsterdam.
Fratantoni, D. M., and P. L. Richardson (2006), The evolution and demise of North Brazil Current rings, *J. Phys. Oceanogr.*, *36*, 1241–1264.
Fu, L.-L. (2006), Pathways of eddies in the South Atlantic Ocean revealed from satellite altimeter observations, *Geophys. Res. Lett.*, *33*, L14610, doi:10.1029/2006GL026245.
Fu, L.-L., and G. R. Flierl (1980), Nonlinear energy and enstrophy transfers in a realistically stratified ocean, *Dyn. Atmos. Oceans*, *4*, 219–246.
Ganachaud, A. (2003), Error budget of inverse box models: The North Atlantic, *J. Atmos. Oceanic Technol.*, *20*, 1641–1655.
Gill, A. E. (1982), *Atmosphere-Ocean Dynamics*, 662 pp., Academic Press, N. Y.
Gill, A. E., and P. P. Niiler (1973), The theory of the seasonal variability in the ocean, *Deep Sea Res. Oceanogr. Abstr.*, *20*, 141–177.
Gregory, J. M., et al. (2005), A model intercomparison of changes in the Atlantic thermohaline circulation in response to increasing atmospheric CO_2 concentration, *Geophys. Res. Lett*, *32*, L12703, doi:10.1029/2005GL023209.
Hall, M. M., and H. L. Bryden (1982), Direct estimates and mechanisms of ocean heat transport, *Deep Sea Res., Part A*, *29*, 339–359.
Halliwell, G. R., P. Cornillon, and D. A. Byrne (1991), Westward-propagating SST anomaly features in the Sargasso Sea, 1982-88, *J. Phys. Oceanogr.*, *21*, 635–649.
Hirschi, J. J.-M., P. D. Killworth, and J. R. Blundell (2007), Subannual, seasonal, and interannual variability of the North Atlantic meridional overturning circulation, *J. Phys. Oceanogr.*, *37*, 246–1265.
Hirschi, J. J.-M., A. T. Blaker, B. Sinha, A. Coward, B. de Cuevas, S. Alderson, and G. Madec (2013), Chaotic variability of the meridional overturning circulation on subannual to interannual timescales, *Ocean Sci.*, *9*, 805–823.
Jochumsen, K., M. Rhein, S. Hüttl-Kabus, and C. W. Böning (2010), On the propagation and decay of North Brazil Current rings, *J. Geophys. Res.*, *115*, C10004, doi:10.1029/2009JC006042.
Johns, W. E., T. Kanzow, and R. Zantopp (2005), Estimating ocean transports with dynamic height moorings: An application in the Atlantic deep western boundary current, *Deep Sea Res., Part I*, *52*, 542–1567.
Johns, W. E., L. M. Beal, M. O. Baringer, J. R. Molina, S. A. Cunningham, T. Kanzow, and D. Rayner (2008), Variability of shallow and deep western boundary currents off the Bahamas during 2004-05: Results from the 26°N RAPID-MOC array, *J. Phys. Oceanogr.*, *38*, 605–623.
Kanzow, T., Cunningham, S. A., Rayner, D., Hirschi, J. J.-M., Johns, W. E., Baringer, M. O., Bryden, H. L., Beal, L. M., Meinen, C. S., and J. Marotzke (2007), Observed flow compensation associated with the MOC at 26.5°N in the Atlantic, *Science*, *317*, 938–941.
Kanzow, T., H. L. Johnson, D. P. Marshall, S. A. Cunningham, J. J.-M. Hirschi, A. Mujahid, H. L. Bryden, and W. E. Johns (2009), Basinwide integrated volume transports in an eddy-filled ocean, *J. Phys. Oceanogr.*, *39*, 3091–3110.
Kanzow, T., et al. (2010), Seasonal variability of the Atlantic meridional overturning circulation at 26.5°N, *J. Clim.*, *23*, 5678–5698.
Killworth, P. D., D. B. Chelton, and R. A. de Szoeke (1997), The speed of observed and theoretical long extratropical planetary waves, *J. Phys. Oceanogr.*, *27*, 1946–1966.
Kundu, P. K., J. S. Allen, and R. L. Smith (1975), Modal decomposition of the velocity field near the Oregon coast, *J. Phys. Oceanogr.*, *5*, 683–704.
Lapeyre, G. (2009), What vertical mode does the altimeter reflect? On the decomposition in baroclinic modes and on a surface-trapped mode, *J. Phys. Oceanogr.*, *39*, 2857–2874.
Lee, T., W. E. Johns, R. Zantopp, and E. Fillenbaum (1996), Moored observations of western boundary current variability and thermohaline circulation at 26.5°N in the subtropical North Atlantic, *J. Phys. Oceanogr.*, *26*, 962–983.
Louis, J. P., and P. C. Smith (1982), The development of the barotropic radiation field of an eddy over a slope, *J. Phys. Oceanogr.*, *12*, 56–73.
Lynn, R. J., and J. L. Reid (1968), Characteristics and circulation of deep and abyssal waters, *Deep Sea Res. Oceanogr. Abstr.*, *15*, 577–598.

Marsh, R., B. A. de Cuevas, A. C. Coward, J Jacquin, J. J.-M. Hirschi, Y. Aksenov, A. J. G. Nurser, and S. A. Josey (2009), Recent changes in the North Atlantic circulation simulated with eddy-permitting and eddy-resolving ocean models, *Ocean Modell.*, *28*, 226–239.
McCarthy, G., E. Frajka-Williams, W. E. Johns, M. O. Baringer, C. S. Meinen, H. L. Bryden, D. Rayner, A. Duchez, C. Roberts, and S. A. Cunningham (2012), Observed interannual variability of the Atlantic meridional overturning circulation at 26.5°N, *Geophys. Res. Lett*, *39*, L19609, doi:10.1029/2012GL052933.
Meinen, C. S., W. E. Johns, S. L. Garzoli, E. V. Sebille, D. Rayner, T. Kanzow, and M. O. Baringer (2013), Variability of the Deep Western Boundary Current at 26.5°N during 2004–2009, *Deep Sea Res., Part II*, *85*, 154–168.
MODE Group (1978), The mid-ocean dynamics experiment, *Deep Sea Res.*, *25*, 859–910.
Osychny, V., and P. Cornillon (2004), Properties of Rossby waves in the North Atlantic estimated from satellite data, *J. Phys. Oceanogr.*, *34*, 61–76.
Parker, C. E. (1971), Gulf Stream rings in the Sargasso Sea, *Deep Sea Res. Oceanogr. Abstr.*, *18*, 981–993.
Percival, D. B., and A. T. Walden (1993), *Spectral Analysis for Physical Applications*, 612 pp., Cambridge Univ. Press, Cambridge, U. K.
Pohlmann, H., F. Sienz, and M. Latif (2006), Influence of the multidecadal Atlantic meridional overturning circulation variability on European climate, *J. Clim.*, *19*, 6062–6067.
Rayner, D., et al. (2011), Monitoring the Atlantic meridional overturning circulation, *Deep Sea Res., Part II*, *58*, 1744–1753.
Rhines, P. B. (1977), The dynamics of unsteady currents, in *The Sea*, vol. 6, pp. 189–318, Wiley Interscience, N. Y.
Richman, J. G., C. Wunsch, and N. G. Hogg (1977), Space and time scales of mesoscale motion in the Western North Atlantic, *Rev. Geophys.*, *15*, 345–420.
Sangrà, P., et al. (2009), The Canary Eddy Corridor: A major pathway for long-lived eddies in the subtropical North Atlantic, *Deep Sea Res., Part I*, *56*, 2100–2114.
Shi, C., and D. Nof (1994), The destruction of lenses and generation of wodons, *J. Phys. Oceanogr.*, *24*, 1120–1136.
Siegel, D. A., D. J. McGillicuddy Jr., and E. A. Fields (1999), Mesoscale eddies, satellite altimetry, and new production in the Sargasso Sea, *J. Geophys. Res.*, *104*, 13,359–13,379.
Sinha, B., B. Topliss, A. T. Blaker, and J. -M Hirschi (2013), A numerical model study of the effects of interannual time scale wave propagation on the predictability of the Atlantic meridional overturning circulation, *J. Geophys. Res. Oceans*, *118*, 1–16, doi:10.1029/2012JC008334.
Smeed, D. A., et al. (2014), Observed decline of the Atlantic meridional overturning circulation 2004–2012, *Ocean Sci.*, *10*, 29–38.
Smith, K. S., and G. K. Vallis (2001), The scales and equilibration of mid-ocean eddies: Freely evolving flow, *J. Phys. Oceanogr.*, *31*, 554–571.
Stammer, D. (1997), Global characteristics of ocean variability estimated from regional TOPEX/POSEIDON altimeter measurements, *J. Phys. Oceanogr.*, *27*, 1743–1769.
Szuts, Z. B., J. R. Blundell, M. P. Chidichimo, and J. Marotzke (2012), A vertical-mode decomposition to investigate low-frequency internal motion across the Atlantic at 26°N, *Ocean Sci.*, *8*, 345–367.
Tailleux, R., and J. McWilliams (2000), Acceleration, creation, and depletion of wind-driven, baroclinic Rossby waves over an ocean ridge, *J. Phys. Oceanogr.*, *30*, 2186–2213.
Treguier, A. M., and B. L. Hua (1988), Influence of bottom topography on stratified quasi-geostrophic turbulence in the ocean, *Geophys. Astrophys. Fluid Dyn.*, *43*, 265–305.
Tulloch, R., J. Marshall, and K. S. Smith (2009), Interpretation of the propagation of surface altimetric observations in terms of planetary waves and geostrophic turbulence, *J. Geophys. Res.*, *114*, C02005, doi:10.1029/2008JC005055.
Wunsch, C. (1997), The vertical partition of oceanic horizontal kinetic energy, *J. Phys. Oceanogr.*, *27*, 1770–1794.
Wunsch, C. (2008), Mass and volume transport variability in an eddy-filled ocean, *Nat. Geosci.*, *1*, 165–168.